The Cryosphere, 9, 255–268, 2015
www.the-cryosphere.net/9/255/2015/
doi:10.5194/tc-9-255-2015

The Cryosphere
Open Access

Regional melt-pond fraction and albedo of thin Arctic first-year drift ice in late summer

D. V. Divine[1,2], M. A. Granskog[1], S. R. Hudson[1], C. A. Pedersen[1], T. I. Karlsen[1], S. A. Divina[1], A. H. H. Renner[1,3], and S. Gerland[1]

[1]Norwegian Polar Institute, Fram Centre, 9296 Tromsø, Norway
[2]Department of Mathematics and Statistics, Faculty of Science and Technology, University of Tromsø, 9037 Tromsø, Norway
[3]Institute of Marine Research, Sykehusveien 23, 9019 Tromsø, Norway

Correspondence to: D. V. Divine (dmitry.divine@npolar.no)

Received: 17 June 2014 – Published in The Cryosphere Discuss.: 11 July 2014
Revised: 26 November 2014 – Accepted: 9 January 2015 – Published: 9 February 2015

Abstract. The paper presents a case study of the regional ($\approx$ 150 km) morphological and optical properties of a relatively thin, 70–90 cm modal thickness, first-year Arctic sea ice pack in an advanced stage of melt. The study combines in situ broadband albedo measurements representative of the four main surface types (bare ice, dark melt ponds, bright melt ponds and open water) and images acquired by a helicopter-borne camera system during ice-survey flights. The data were collected during the 8-day ICE12 drift experiment carried out by the Norwegian Polar Institute in the Arctic, north of Svalbard at 82.3° N, from 26 July to 3 August 2012. A set of $>$ 10 000 classified images covering about 28 km^2 revealed a homogeneous melt across the study area with melt-pond coverage of $\approx$ 0.29 and open-water fraction of $\approx$ 0.11. A decrease in pond fractions observed in the 30 km marginal ice zone (MIZ) occurred in parallel with an increase in open-water coverage. The moving block bootstrap technique applied to sequences of classified sea-ice images and albedo of the four surface types yielded a regional albedo estimate of 0.37 (0.35; 0.40) and regional sea-ice albedo of 0.44 (0.42; 0.46). Random sampling from the set of classified images allowed assessment of the aggregate scale of at least 0.7 km^2 for the study area. For the current setup configuration it implies a minimum set of 300 images to process in order to gain adequate statistics on the state of the ice cover. Variance analysis also emphasized the importance of longer series of in situ albedo measurements conducted for each surface type when performing regional upscaling. The uncertainty in the mean estimates of surface type albedo from in situ measurements contributed up to 95 % of the variance of the estimated regional albedo, with the remaining variance resulting from the spatial inhomogeneity of sea-ice cover.

1 Introduction

A new thin-ice Arctic system requires reconsideration of the set of parameterizations of mass and energy exchange within the atmosphere–sea ice–ocean system used in modern coupled general circulation models (CGCMs) including Earth system models. Such a reassessment would require a comprehensive collection of measurements made specifically on first-year pack ice with a focus on the summer melt season, when the difference from typical conditions for the earlier multiyear Arctic sea-ice cover becomes most pronounced (Perovich et al., 2002a; Grenfell and Perovich, 2004; Perovich and Polashenski, 2012).

Surface albedo is one of the major physical quantities controlling the intensity of the energy exchange at the atmosphere–sea ice–ocean interface and the heat balance of sea ice (e.g., Doronin and Kheisin, 1977; Maykut, 1982; Curry et al., 1995). Knowledge of the surface albedo for different types of sea ice, as well as its spatial and seasonal variability, is crucial for obtaining adequate representations of the sea-ice cycle in the CGCMs (e.g., Holland et al., 2012; Björk et al., 2013; Karlsson and Svensson, 2013).

During summer, the net positive heat balance of sea ice causes substantial transformation in the state of the ice cover. Water runoff from melting snow and upper ice layers tends to form puddles in depressions in the sea-ice surface (e.g.,

Zubov, 1945; Untersteiner, 1961; Nazintsev, 1964; Fetterer and Untersteiner, 1998). These melt ponds spread rapidly and, on level first-year ice (FYI), can cover up to 75 % of the surface during the initial stage of surface melt (Hanesiak et al., 2001; Grenfell and Perovich, 2004; Polashenski et al., 2012). As the albedo of a melt pond is markedly lower than that of the bare or snow-covered sea ice (e.g., Doronin and Kheisin, 1977; Grenfell and Maykut, 1977; Fetterer and Untersteiner, 1998; Perovich et al., 2002b; Grenfell and Perovich, 2004), the spatial distribution of melt ponds and leads has clear implications for the spatial aggregate albedo (Perovich, 2005) and accelerated summer decay of sea ice.

Field observations suggest a pronounced difference in the seasonal evolution of first-year sea-ice albedo compared with that of multiyear ice. The surface of multiyear sea ice typically features more rough topography and thicker snow cover, leading to a limited potential melt-pond coverage (e.g., Eicken et al., 2002, 2004; Perovich and Polashenski, 2012). Thicker ice underneath the melt-pond bottom leads to generally higher spatial albedo, lower transmission and lower energy absorption on melting multiyear ice (Eicken et al., 2002; Perovich, 2005; Hudson et al., 2013; Nicolaus et al., 2012). As a result, the summer albedo of multiyear ice cover is systematically higher than that of younger ice throughout the entire melt season, inducing an additional ice age–albedo feedback (Perovich and Polashenski, 2012).

The relatively small spatial scale of a typical pond system, typically few tens to thousands of m^2 (e.g., Tschudi et al., 2001; Perovich et al., 2002b; Hohenegger et al., 2012), large intersite variability in melt-pond coverage and the overcast conditions prevailing in the summer Arctic promote the use of low-altitude airborne methods for studying the morphological and optical properties of the sea-ice cover. Although remote sensing of summer sea ice utilizing various satellite-based sensors has made considerable progress throughout the last decades (e.g., Markus et al., 2003; Rösel et al., 2012; Tschudi et al., 2008; Kim et al., 2013), these aerial surveys can provide valuable high-resolution validation data for the emerging algorithms. Combining the spatial data on surface types with in situ measurements of incident/reflected solar radiation (albedo) and turbulent heat fluxes for different types of surfaces may in turn provide estimates of the regional-scale surface energy balance of sea ice. A number of such studies have been conducted in the past with a focus on spatial and temporal evolution of fractional melt-pond coverage, pond-size probability density (e.g., see Perovich et al., 2002b, for a review), and their relationship with the pre-melt surface topography (Derksen et al., 1997; Eicken et al., 2004; Petrich et al., 2012) and surface albedo. Depending on the instrumentation setup used, the spatial ranges covered varied from tens of meters to hundreds of kilometers, on the order of the typical scale of a GCM grid cell.

Safety and logistical challenges associated with these types of studies result in the relevant surface-based field data preferentially representing thicker first-year sea ice at the initial stages of melt and/or sea ice from coastal areas, where the sediment load may modify the spectral albedo and melt pattern. Limited data exist for thinner, less than 1 m thick, Arctic first-year ice that is expected to occupy a substantial part of the Arctic basin in the future if (and when) the projected transition to a nearly seasonal ice cover has occurred.

A comprehensive set of observations of the energy balance of melting Arctic first-year sea ice was conducted during an 8-day ice station in July–August 2012. Hudson et al. (2013) presented results from in situ measurements obtained during the drift experiment. This paper shows the analysis of the regional morphological properties of the sea-ice surface, inferred from aerial surveys. The in situ measurements of broadband albedo and the derived regional spatial distribution of surface types are used to obtain an estimate of the regional albedo of Arctic first-year ice in the advanced stage of melt. The upscaling scheme applied in the study treats all major observed quantities as random variables. Corroborated with the respective areal data on sea-ice thickness, the analysis provides the probability density functions on the regional albedo together with the albedo of thin (70–90 cm) first-year ice with a well-developed melt-pond cover.

The paper is organized as follows. Section 2 presents the geographical setting, instrument setup, image-processing techniques, details on the upscaling technique applied and uncertainties in the key variables we used for estimating the regional albedo. Section 3.1 shows the spatial variability of melt-pond and open-water fractions inferred from six helicopter ice-survey flights. The along-track albedo variability and the regional and sea-ice albedo estimates are then presented in Sect. 3.2. Finally the results of the work are discussed and summarized in Sect. 4.

2 Data and methods

2.1 ICE12 drift experiment

The energy balance of melting thin first-year Arctic sea ice was a focus of the 8-day ICE12 drifting ice floe experiment on R/V *Lance*, conducted from 26 July to 3 August 2012, north of Svalbard in the southwestern Nansen Basin (82.3° N, 21.5° E). Figure 1 shows the *Lance* drift track that was in an area of very close (≥ 90 %) drift ice. The corresponding operational ice chart produced by the Norwegian Ice Service of the Norwegian Meteorological Institute (NMI, www.met.no) from 1 August is shown superimposed onto the map. The ice floe (ICE12 floe hereafter) that *Lance* was moored to during the drift had a size of approximately $\varnothing$ 600 m and a modal ice thickness of 0.8 m, deducted from drillings and measurements using a Geonics EM-31 electromagnetic induction device (Hudson et al., 2013). The floe was mainly represented by level ice, with ridging over less than 10 % of the area. Based on airborne surveys of ice thickness using another electromagnetic induction device, the EM

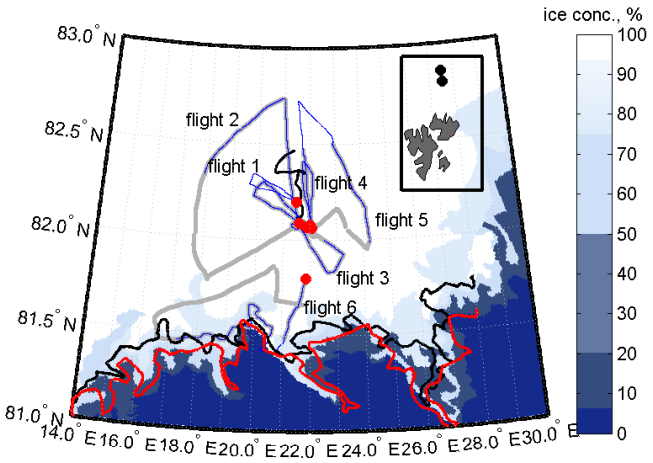

Figure 1. Map of the study area showing the track of the ICE12 floe during the drift north of Svalbard from 26 July to 3 August 2012 (solid black line); an inset map in the upper right corner also shows the start and end drift coordinates relative to the Svalbard archipelago. The black and red curves outline the ice edge on 2 days, 31 July and 2 August, defined as 40 % ice concentration based on ice charts from the Norwegian Meteorological Institute (NMI). The NMI ice chart from 1 August is shown as the reference. The grey and blue lines show the segments of six helicopter ice-reconnaissance flight tracks with EM bird and ICE camera data, respectively (see Table 1). Red dots mark the starting points for the flights.

bird (Haas et al., 2009), and analysis of aerial photography, the floe was found to be representative for the area. The sea ice was in the latter stage of melt, covered by melt ponds some 15–30 cm deep with steep margins. The majority of ponds were connected to complex networks, often with an outlet to the ocean. Some of the ponds had actually melted through the ice slab, corresponding to stage III of surface-melt and melt-pond evolution according Eicken et al. (2002).

2.1.1 In situ broadband albedo measurements

The broadband albedo of the sea-ice surface was measured in situ during the ICE12 drift experiment using a mobile instrument platform for measuring the radiation budget on sea ice (Hudson et al., 2012, 2013). Observations of the surface radiative fluxes were done on seven representative transects with a 5 m interval over a total of 490 m. Hudson et al. (2013), using the surface type classification technique from Renner et al. (2013), discriminated between four major types of sea-ice surface in the ICE12 floe area: open water and bare ice and dark and bright ponds. The latter refers to light blue ponds with thicker, more reflective ice underneath. The measurements were grouped according to the surface types to yield the mean albedos for the dark ponds $\overline{\alpha_{\mathrm{dp}}} = 0.15$ and light ponds $\overline{\alpha_{\mathrm{bp}}} = 0.34$, respectively, and of bare white ice $\overline{\alpha_{\mathrm{bi}}} = 0.55$ (see Table 1 in Hudson et al., 2013, for more details and Table S1 in the Supplement presented here). The albedo of open water/leads was set to the commonly used $\overline{\alpha_{\mathrm{ow}}} = 0.066$ (Pegau and Paulson, 2001). We note that cloudy conditions prevailed during the drift experiment, ensuring relative homogeneity in illumination in the study area.

2.1.2 Low-altitude imagery of sea ice during ICE12 experiment

The imaging of the sea-ice surface during the cruise was done using a recently designed ICE camera system mounted on a Eurocopter AS-350 helicopter. The hardware component of the system includes two downward-facing Canon EOS 5D Mark II digital photo cameras equipped with Canon 20 mm f/2.8 USM lenses, a combined SPAN-CPT GPS/INS unit by Novatel and LDM301 by Jenoptik, a laser distance measurement device used as an altimeter in the setup. These components were housed in a single aerodynamic enclosure and mounted outside the helicopter. The single-point horizontal positioning accuracy for the system was within 1.5 m, and the uncertainty in the altitude over the sea ice was estimated to be < 0.3 m, which corresponds to a typical scale of sea-ice draft variability.

Since the ICE camera was designed as a component of a photogrammetric setup, the image shooting rate was set to one frame per second per camera yielding two captured images per second. This was sufficient to ensure about 50–70 % overlap between successive images for flights at an altitude of 35–40 m and with a velocity of 30–40 m s^{-1} – parameters typical for EM bird flights. We fixed the camera lenses' focal lengths to infinity. For every captured image, the position, attitude and altitude of the event were logged in the system. The cameras' own 128 GB compact flash cards stored the captured images; the card size was sufficient for the system to shoot continuously for about 1 h, taking about 4500 images per camera in raw Canon format. A subset of some 10 300 images with minimal (< 10 %) or no overlap captured during six longer survey flights was selected for further processing and used in the presented study. To form this subset, every second image from one of the cameras was used. Figure 1 shows the selected flight tracks. Results of the data analysis from these flights together with in situ observations are reported below and also summarized in Tables 1 and 2.

2.1.3 Image and navigation data processing

For a typical flight altitude of about 35 m over the sea ice, the camera lenses used in the setup provide a footprint of about 60 by 40 m. With the image sensor geometry at its native resolution this corresponds to a pixel size on the ground of about 1 cm. For typical helicopter roll (pitch) angles of about $-2°$ ($1°$), the distortion of the image plane from an ideal rectangular one and the associated uncertainty in the image area of less than 1 % was considered insignificant; therefore no correction for pitch and roll was applied to the images.

Table 1. Summary statistics on the state of sea-ice cover along the six processed helicopter flight tracks from the ICE12 cruise. The open-water coverage f^{s}_{ow} and melt-pond fraction f^{s}_{mp} (relative to sea-ice area) are the whole swath-based estimates rather than averages of the respective values from individual images presented in the corresponding figures. The values of f^{s}_{ow} and f^{s}_{mp} for flight 2, shown in parentheses, are the respective estimates based on the images processed using the method of Renner et al. (2013). The bottom entry shows the regional aggregate values derived from flights 1–5.

Flight number	Date	GMT start–end times	N images	Transect length (area), km (km^2)	f^{s}_{ow} %	f^{s}_{mp} %
1	31.07.12	7:36–8:10	1031	67 (2.4)	7	26
2	01.08.12	7:22–8:34	1902	139 (5.0)	10 (9)	24 (27)
3	01.08.12	16:45–18:03	2237	154 (5.7)	14	25
4	02.08.12	11:21–12:00	993	78 (2.5)	14	24
5	02.08.12	13:21–14:45	2121	170 (5.2)	12	26
6	03.08.12	14:43–16:04	1979	165 (7.4)	30	20
Regional aggregate	–	–	8284	608 (20.8)	12	25

Table 2. Summary statistics on the aggregate surface albedo α^{s} and sea-ice albedo α^{s}_{si} along the six processed helicopter flight tracks from the ICE12 cruise and the respective regional estimates α^{r} and α^{r}_{si}. The total regional albedo is calculated with and without flight 6 data taken into account. The numbers in parentheses in the albedo column denote the respective block bootstrap 95 % confidence interval on the estimates.

Flight number	Aggregate albedo (α^{s})	Aggregate albedo sea ice (α^{s}_{si})
1	0.41 (0.39; 0.43)	0.44 (0.42; 0.46)
2	0.40 (0.38; 0.43)	0.45 (0.42; 0.47)
3	0.38 (0.36; 0.41)	0.44 (0.41; 0.46)
4	0.39 (0.36; 0.41	0.44 (0.42; 0.46)
5	0.39 (0.37; 0.41)	0.44 (0.41; 0.46)
6	0.32 (0.29; 0.35)	0.44 (0.42; 0.47))
α^{r} (1–5)	0.39 (0.37; 0.41)	–
α^{r} (1–6)	0.37 (0.35; 0.40)	–
α^{r}_{si} (1–6)	–	0.44 (0.42; 0.46)

Image correction for camera lens distortion is necessary prior to any further analysis of the acquired images. We used generic lens correction and vignetting correction procedures with a polynomial lens distortion model implemented in Adobe Lightroom® software.

The large array of data to be analyzed promoted the use of a simplified image-processing technique. In order to discriminate between open water, bare ice and melt ponds, we applied a three-step object identification and classification procedure. This involved:

a. image segmentation/binarization using Otsu's method, which chooses the threshold to minimize the intra-class variance of the black and white pixels (Otsu, 1979);

b. boundary tracing on the binarized images by the Moore–Neighbor tracing algorithm modified by Jacob's stopping criteria (Gonzalez etal., 2010);

c. object classification (open water, bare ice or melt pond) using thresholding in the red channel intensity.

Due to the relatively high contrasts between the different surface types during summer melt, this relatively simplistic approach appeared to work well with a minimum of supervision required during the processing of the sequences of images captured by the camera system. All procedures were implemented in Matlab using the "image processing" toolbox (MATLAB, 2012).

For each flight track of length N images, the method yielded the series of $\left\{f^{i}_{mp}, f^{i}_{ow}, S^{i}\right\}$, $i = 1, \ldots, N$, with f^{i}_{mp} denoting the image fractional melt-pond coverage with respect to the sea-ice area, f^{i}_{ow} the open-water fraction and S^{i} standing for the respective area of image i. Figure 2 demonstrates an example of the object classification procedure for an image captured during flight 1 (Table 1). The edges of the melt-pond objects are accurately identified. Note that we left out the darker objects with an area less than 0.5 m^2 because the contribution of these objects to the total melt-pond coverage was found to be negligible. The identified set of objects of three types is then used for calculating along the track summary statistics on melt-pond coverage and open-water fraction. The parts of the image not classified as melt ponds or open water were considered as bare sea ice. For the case in Fig. 2, f_{ow} was calculated to be 8 % and f_{mp} was 16 % with respect to the total sea-ice area.

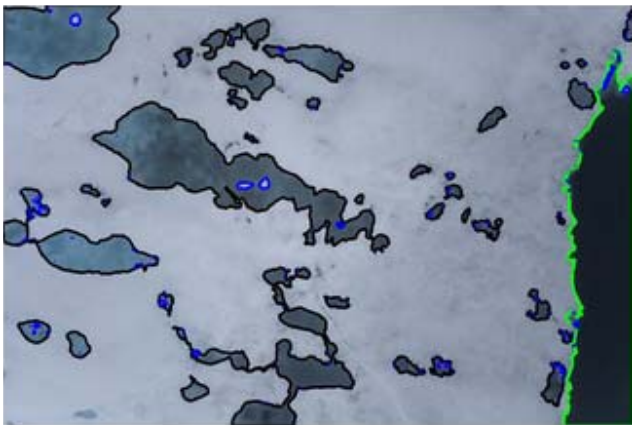

Figure 2. Example of the image segmentation procedure showing an image captured during flight 1 from an altitude of 35 m. The dimensions of the scene are 60.5 by 40.5 m. Black contours highlight the edges of melt ponds; the green contour outlines the open-water area; blue is for the smaller patches of sea ice within melt-pond/open-water objects. For this particular scene the melt-pond fraction f_{mp} (relative to sea-ice area) and open-water fraction f_{ow} are 16 and 8 %, respectively.

2.2 Accounting for uncertainties in the variables used

2.2.1 Error models for melt-pond and open-water fractional coverage

Error models on f_{mp} and f_{ow} are built on the additional analysis of 1622 images from flight 2 using the classification method of Renner et al. (2013). The technique involves a semi-automated surface type classification and manual supervision of the processed images, allowing more reliable results at the cost of increased labor intensity. Processing of the images used in this verification procedure yielded the image-based fractional coverage of the four surface classes: dark ponds, bright ponds, open water and bare ice. This data set was used as a reference to estimate the uncertainty in the corresponding quantities derived from the larger image set and to assess the probability density of the ratio of the areas of dark to bright ponds at the regional scale.

Imagewise intercomparison of f_{mp} and f_{ow} values demonstrated an average bias of f^{b}=0.03, with $\sigma_{f^{\mathrm{b}}}$=0.04 in the fraction of melt ponds between the images processed using the technique of Renner et al. (2013) and the simplified approach applied in this study. Inspection of images revealed that the algorithm presented in Sect. 2.1.3 sometimes underestimates the melt-pond coverage by identifying some bright ponds as bare white ice. Likewise, some of the darkest melt ponds were sometimes misidentified as open water/leads. The error model for f^i_{mp} and f^i_{ow} of an image i is therefore defined as

$$\left\{p(f^i_{\mathrm{mp}}),\ p(f^i_{\mathrm{ow}})\right\} = \tag{1}$$
$$\begin{cases} p(f^i_{\mathrm{mp}}) \sim p(f^i_{\mathrm{mp}} + \mathcal{N}(f^{\mathrm{b}}, \sigma^2_{f^{\mathrm{b}}}) \,|\, \mathcal{N}(f^{\mathrm{b}}, \sigma^2_{f^{\mathrm{b}}}) \geq 0) \\ p(f^i_{\mathrm{ow}}) \sim p(f^i_{\mathrm{ow}} - (1 - f^i_{\mathrm{ow}})\mathcal{N}(f^{\mathrm{b}}, \sigma^2_{f^{\mathrm{b}}}) \,|\, \mathcal{N}(f^{\mathrm{b}}, \sigma^2_{f^{\mathrm{b}}}) < 0) \end{cases},$$

where parameters of the Gaussian distribution were estimated from the data.

The areal ratio of dark to bright ponds, r, was estimated using a bootstrap technique (Efron and Tibshirani, 1993) involving sampling with replacement from the same complementary data set of classified images, followed by a re-estimation of the sought r for each bootstrap replicate. The proportion of the drawn to the replaced data points (i.e., classified images) within each replicate was set to $2/1$ with all the images being equally weighted. The resulting distribution of the mean areal r derived from 10 000 replicates was approximated by a Gaussian probability density function (pdf) with $p(r) \sim \mathcal{N}(2.8, 0.15^2)$.

2.2.2 In situ broadband albedo as a random variable

Uncertainties in the average in situ albedo $\overline{\alpha_j}$ are estimated empirically from available data for each surface type j. During the ICE12 experiment we obtained 50 individual albedo measurements over bare white ice, 12 over dark melt ponds and 1 over a bright pond. This yields sample standard deviations (SDs), $\sigma^{\mathrm{sp}}_{\alpha}$, on single point measurements of 0.05 and 0.04 for bare white ice and dark ponds, respectively (see Table S1 for details). Using a simplistic error model assuming independent measurements with random Gaussian errors, we calculate the uncertainty of the measurement-based average albedo of surface type j as

$$\sigma_{\overline{\alpha_j}} = \frac{\sigma^{\mathrm{sp}}_{\alpha_j}}{\sqrt{m_j}} + \frac{\sigma^{\mathrm{ins}}_{\alpha_j}}{\sqrt{m_j}}, \tag{2}$$

where m_j refers to the number of available albedo measurements in the surface type under consideration. The single measurement instrumental error, $\sigma^{\mathrm{ins}}_{\alpha_j}$, was set to $0.1\overline{\alpha_j}$, where the coefficient 0.1 stems from a declared 5 % measurement uncertainty yielding a total uncertainty of 10 % for the ratio of reflected-to-incoming radiation (i.e., albedo), again assuming the errors are independent. For the "bright pond" category, where only one albedo measurement was available with no significant influence from other surface types, we assigned an uncertainty of $0.1\overline{\alpha_{\mathrm{bp}}}$ although we acknowledge that this value can be a biased estimate. For the open-water albedo uncertainty, a value of 0.0066, derived from 24 measurements, was adopted from Pegau and Paulson (2001). Table S1 shows the resulting values of $\sigma_{\overline{\alpha_j}}$ for the four surface classes. The mean albedo of every surface type j can now be considered as a t-distributed random variable with m_j degrees of freedom, distributed as $p(\overline{\alpha_j}) \sim \overline{\alpha_j} + t_{m_j}\sigma_{\overline{\alpha_j}}$.

The use of t-distribution accounts for a larger spread in the estimate of the true mean when dealing with the relatively small sample sizes. For bright ponds, the Gaussian approximation was used instead to prevent the occasional generation of albedo values outside the admissible range of $[0, 1]$ due to heavy tails of the t-distribution with one degree of freedom.

This approach should be considered a simplification, as it reduces the whole variety of surface types with different optical characteristic to only four major surface types. However we expect that the imposed range of random variability in a particular surface-type albedo covers the natural variation of this parameter, thereby accounting indirectly for the effects of numerous additional factors like the thickness of ice, surface-state and small-scale morphology, pond depth and ice thickness beneath the pond as well as changing light conditions.

2.3 Bootstrap aggregate albedo

The aggregate albedo of a spatial mosaic of surface types is generally defined as (Perovich, 2005)

$$\alpha = g(\alpha_j, f_j) := \sum_j \alpha_j f_j;\ \{\alpha_j, f_j\} \in [0, 1], \tag{3}$$

where summation is over all surface types used, here $j = \{\mathrm{ow}, \mathrm{bi}, \mathrm{bp}, \mathrm{dp}\}$, with the corresponding fractional coverage f_j. Note that for convenience we use the fractional total melt-pond coverage, f_{mp}, relative to the sea-ice area. Coefficients f_{bp} and f_{dp} are defined as fractions of bright and dark melt ponds with regard to the relative melt-pond coverage, i.e., $f_{\mathrm{bp}} = (1/(1+r))\, f_{\mathrm{mp}}$ and $f_{\mathrm{dp}} = (r/(1+r))\, f_{\mathrm{mp}}$. This transforms Eq. 3 for α to

$$\begin{aligned}\alpha &= \alpha_{\mathrm{ow}} f_{\mathrm{ow}} + \alpha_{\mathrm{bi}}(1 - f_{\mathrm{mp}})(1 - f_{\mathrm{ow}}) + \\ &+ \alpha_{\mathrm{bp}} f_{\mathrm{bp}}(1 - f_{\mathrm{ow}}) + \alpha_{\mathrm{dp}} f_{\mathrm{dp}}(1 - f_{\mathrm{ow}}).\end{aligned} \tag{4}$$

For any arbitrary set $\left\{f^i_{\mathrm{mp}}, f^i_{\mathrm{ow}}, S^i\right\}$, $i = 1, \ldots, N$, the set-based aggregate albedo α^{s} is therefore calculated in the same way as the local estimate using Eq. 4, with the values of $f^{\mathrm{s}}_{\mathrm{ow}}$ and $f^{\mathrm{s}}_{\mathrm{mp}}$ derived as

$$\begin{aligned} f^{\mathrm{s}}_{\mathrm{ow}} &= \sum_i S^i f^i_{\mathrm{ow}} / \sum_i S^i \\ f^{\mathrm{s}}_{\mathrm{mp}} &= \sum_i S^i (1 - f^i_{\mathrm{ow}}) f^i_{\mathrm{mp}} / \sum_i S^i \end{aligned}$$

and referring to the set-based estimates of open-water and melt-pond fractions.

Deriving particular values of interest from the analysis of individual sea-ice images is analogous to sampling from a random data field with an a priori unknown theoretical distribution and a covariance structure. Any empirical statistic calculated from a set of analyzed images is therefore a derivative of the available data sample and should be considered an estimate accurate to within some unknown probability density.

Since the probability distribution of the local, image-based albedo α^i is non-Gaussian, the large number of available samples makes the bootstrapping (i.e., sampling with replacement) technique (Efron and Tibshirani, 1993) an optimal choice to assess the probability density and the accuracy of the estimated image-set albedo. In our setting, the sets are formed of the swaths of images prone to the presence of autocorrelation in the variables used. It suggests the use of the moving block bootstrap approach (Kunsch, 1989).

For each flight the application of this method to the sequence of $\left\{f^i_{\mathrm{ow}},\ f^i_{\mathrm{mp}},\ S^i\right\}$ involves the following steps:

1. The series of $\left\{f^i_{\mathrm{ow}},\ f^i_{\mathrm{mp}},\ S^i\right\}$ of length N is split into $N - K + 1$ overlapping blocks of length K; the block length is determined empirically from the data using the procedure described in the next subsection.

2. N/K blocks are drawn at random, with replacement, from the constructed set of $N - K + 1$ blocks, and their sequence numbers are registered.

3. M bootstrap samples are drawn from the subset of N/K blocks; albedo for the four different surface types and the values for f^i_{ow}, f^i_{mp} and r can at this step be drawn at random from the respective probability distributions defined in Sects. 2.2.1 and 2.2.2; the set- or swath-based albedo α^{s} is then calculated for each sample using Eq. 4.

Steps 2–3 are repeated L times to generate $L \times M$ estimates of the swath-based aggregate albedo α^{s}. The assigned values of $\{L, M\} = 200$ yield a total of 40 000 samples of α^{s} combined to generate the bootstrap pdf of the swath-based α^{s}. The 95 % confidence interval ($\mathrm{CI}_{0.95}$) on the estimate is then calculated as $\{2.5, 97.5\}$ % of the empirical bootstrap pdf of α^{s}.

2.3.1 Estimating the image block length K using the Markov chain

Accounting for the autocovariance in the analyzed data is implemented following the Nychka et al. (2000) modification of the Mitchell et al. (1966) formula

$$N_{\mathrm{eff}} = N \frac{1 - \phi - 0.68/\sqrt{N}}{1 + \phi + 0.68/\sqrt{N}}, \tag{5}$$

where N_{eff} stands for the effective number of degrees of freedom ("effective sample size"); in general, $N_{\mathrm{eff}} < N$ due to the presence of autocorrelation in a series. This approach implicitly assumes that the analyzed sequence can be adequately described as a realization of the discrete first-order autoregressive process with the autoregressive parameter ϕ.

For each classified image i treated as an individual data sample, further categorization into "ice" or "open water" was

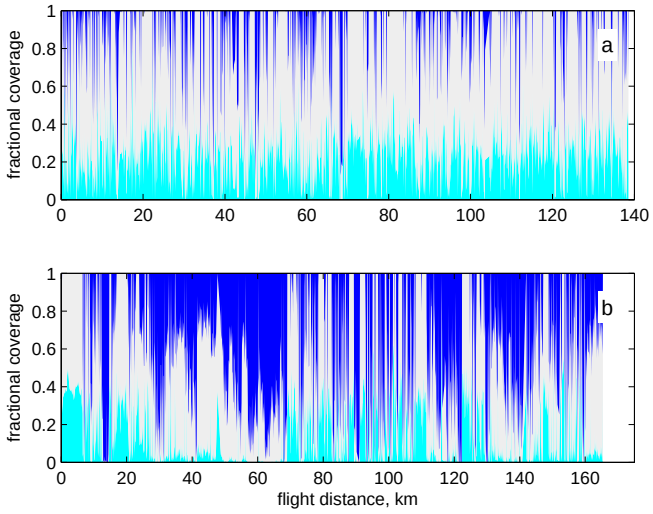

Figure 3. Along-track distribution of fractional melt-pond coverage f^i_{mp} (light blue), bare ice f^i_{bi} (light grey) and open-water fraction f^i_{ow} (blue), all relative to the image area, for flights 2 (very close drift ice, **a**) and 6 (marginal ice zone, **b**). With a swath width of 35–40 m, the covered area corresponds to roughly 0.35–0.40 km^2 per 10 km flight track.

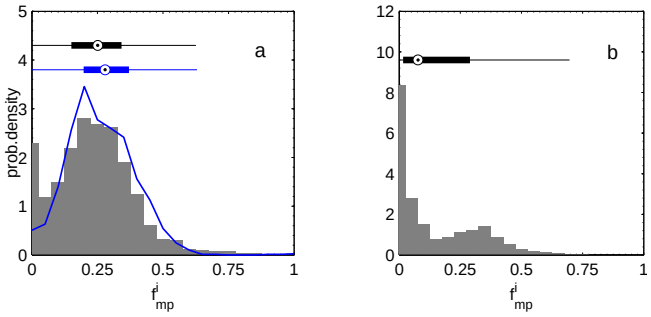

Figure 4. Empirical probability density of f^i_{mp} along the flight tracks 2 **(a)** and 6 **(b)** relative to the sea-ice area. For flight 2 image-based mean f_{mp} of 25 % and the quartiles $Q_{1,2,3}$ of 15, 25 and 34 %, respectively, as shown by the box plot, image-averaged $f_{\mathrm{ow}} =$ 9 %. The blue line and blue box plot in **(a)** show the estimates of the same quantities of $f_{\mathrm{mp}} = 28$ % and $Q_{1,2,3} = \{19, 28, 37\}$ from flight 2 images processed using the method of Renner et al. (2013). For flight 6 image-based mean $f_{\mathrm{mp}} = 15$ % and $Q_{1,2,3} = \{1, 7, 28\}$, image-averaged $f_{\mathrm{ow}} = 37$ %. The whiskers on box plot highlight the 1.5 times interquartile range to cover some 99 % of the observations in total.

applied. Such binarization into the two major surface classes is related to their dominant contribution to the swath-based albedo variance. The images within one flight track that have both open water and sea ice are categorized using a threshold in local open-water fraction. The value for the threshold $f^{\mathrm{t}}_{\mathrm{ow}}$ was set to 5 %, which for the typical flight altitude would correspond to an opening in sea-ice cover at least a few meters wide, i.e., a very small fracture according to WMO sea-ice nomenclature (World Meteorological Organization, 1970).

Fitting the Markov chain of first-order to the derived binary sequence of surface states comprising one complete flight yields the transition matrix **T**. Its largest entry, which in our case characterizes the likelihood of retaining the "ice" state between two successive images, is used as the sought parameter ϕ – a simplistic metric of spatial autocorrelation in the surface state for the analyzed flight track.

3 Results and discussion

3.1 Regional melt-pond coverage and open-water distribution during ICE12 drift

This section presents the results of the analysis of sea-ice imagery along the six selected flight tracks that took place during the ICE12 cruise (Table 1). All but one flight (flight 1, on 31 July) were combined EM bird/ICE camera flights, which fixed the helicopter flight altitude to approximately 35 m above the sea-ice surface except for some shorter periods of climbing to 150–200 m for EM bird calibration.

Figures 3 and 4 show the summary statistics of melt-pond and sea-ice/open-water fractions along the tracks of flights 2 and 6, derived using the technique presented in Sect. 2.1.3. The data for the other four flights are presented in the Supplement in Figs. S1, S3, S5 and S7. Note that for flights 1–5, carried out from 31 July to 2 August, the results are similar, with a typical f_{mp} of about 26 % relative to the sea-ice area and a similarity in the shapes of the respective pdf. In 50 % of these images, the observed f_{mp} was between 15 and 36 %. We found that in some occasions the melt ponds could cover as much as 66 % of the ice surface within the image frame, yet for some 10 % of images with sea ice in the field of view, the sea-ice surface exhibited no or very little melt-pond coverage ($f^i_{\mathrm{mp}} < 4$ %). The average open-water fraction of $f^i_{\mathrm{ow}} = 11$ % was characteristic of very close drift ice and varied for the analyzed images between 0 and 8 % in 50 % of cases, with fewer than 1 % of images showing 100 % open water. This variability lies within the uncertainty of the estimates and corresponds well to the respective operational ice charts for the area (see Fig. 1).

Flight 6, on 3 August, was conducted while moving southwards out of the close drift ice. The flight track traversed the marginal ice zone (MIZ) with extensive areas/strips of open water. Thus the estimates of f_{ow} (30 %) and f_{mp} (20 %) for flight 6 are substantially different from those inferred from survey flights conducted the previous days in the close pack ice (see Fig. 4).

The EM bird surveys conducted during flights 2–6 further corroborate the inference of regional-scale homogeneity in the properties of the sea-ice cover. The probability density functions on sea-ice thickness presented in Fig. 5 suggest fairly similar shapes of the distributions, with the modal ice

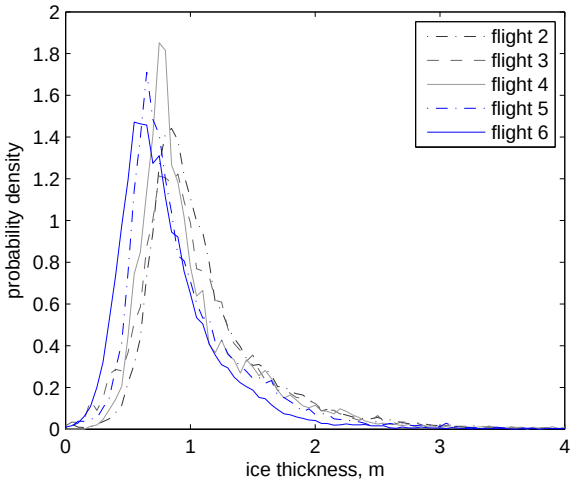

Figure 5. Probability density on sea-ice thickness for flights 2–6 derived from EM bird measurements.

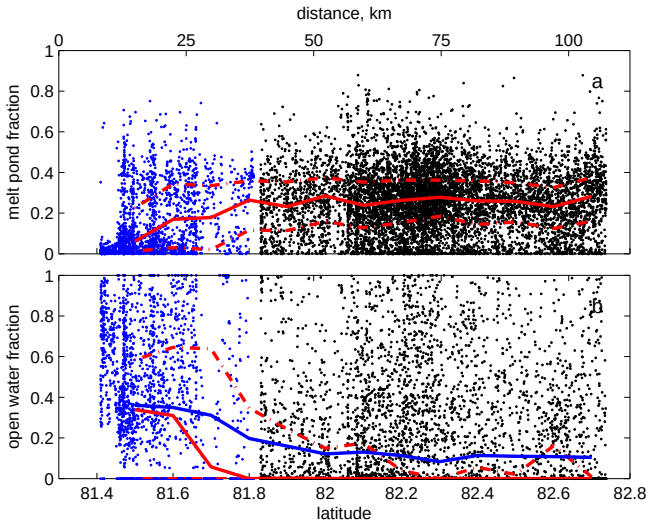

Figure 6. Latitudinal distribution in f^i_{mp} **(a)** and f^i_{ow} **(b)** summarized from the six flight tracks. Black dots highlight the f^i_{mp} and f^i_{ow} inferred from analysis of imagery from flights 1–5; blue dots are for the corresponding values from flight 6. Red solid and dashed lines show the moving median and the quartiles $Q_{1,3}$, respectively, estimated in the window of 0.1° latitude width. For comparison the blue line in **(b)** also shows the moving average to highlight the skewness of the respective image-based probability density.

thickness ranging within 0.7–0.9 m for flights 2–5. The pdf for flight 6 reveals a tendency towards generally thinner ice, with a modal ice thickness of about 0.6 m. We note, however, that there can be a negative bias associated with a much higher open-water coverage observed during this flight.

Figure 6 summarizes the latitudinal distribution in melt-pond fraction and open-water coverage in the study area. Due to the nearly east–west orientation of the MIZ within the study area, Fig. 6 reflects the variability in these parameters towards the sea-ice edge. We note that in the time between the first and fifth flights the ice drifted southwards some 20 km, somewhat smearing the actual distribution in this direction. Flight 6 in turn provided a snapshot across the marginal ice zone. The figure reveals a fairly stable melt-pond coverage across a range of latitudes associated with very close drift ice during the experiment. In the $\approx$30 km wide MIZ the melt-pond coverage shows a gradual decline to values below 10 % close to the edge of the ice pack, in parallel with an increase in the open-water fraction. The transition occurs when the mean open-water fraction exceeds a threshold of approximately 20 % and is most likely associated with a generally more intense melt and a decrease in the typical ice floe size in the area. As the ice floes tend to break up preferentially along the existing melt ponds and melt channels, subsequent transformation of ponds into open water leads to a decreased f_{mp} in the MIZ.

3.2 Bootstrap swath-based and regional albedo estimates

The bootstrap technique described in Sect. 2.3 is applied to the flight-track data of surface type variability $\left\{f^i_{\mathrm{mp}},\ f^i_{\mathrm{ow}},\ S^i\right\}$, $i = 1, \ldots, N$ and in situ albedo measurements from the ICE12 drift experiment to yield the upscaled estimates of swath-based α^{s} and a regional albedo of the study area α^{r}. In addition we use the same technique to calculate the albedo of the ponded sea ice alone (α^{si}). Figures 7a and 8a show local (i.e., based on individual images) aggregate albedo estimates, α^i, made from the helicopter imagery along the two selected flights with contrasting surface conditions presented in Sect. 3.1. The results for other tracks are presented in the Supplement and further summarized in Table 2. Note that in this case the image-based albedo variability is estimated from the data treated "as is" without taking the uncertainties into account.

Figure 7b and corresponding figures in the Supplement demonstrate fairly similar pdfs of local aggregate surface albedo for the flight tracks 1–5, suggesting a homogeneous state of sea-ice cover in the area within approximately 80 km of the ICE12 floe. We note that the empirical probability density functions of local albedo are skewed substantially towards zero due to the contribution of open-water areas. This suggests that an estimate of the regional-scale albedo of melting sea ice pack made by simple averaging of the respective quantities from a sequence of local scenes can be negatively biased. This may have implications for areal estimates of the surface energy budget both in observational and modeling studies.

Panels c in Figs. 7, 8, S2, S4, S6 and S8 display the generated bootstrap probability density of the swath-based α^{s} for the six flights. Table 2 shows the calculated values of the average swath-based albedos and their respective bootstrap $\mathrm{CI}_{0.95}$. The respective values of ϕ from the transition matrix

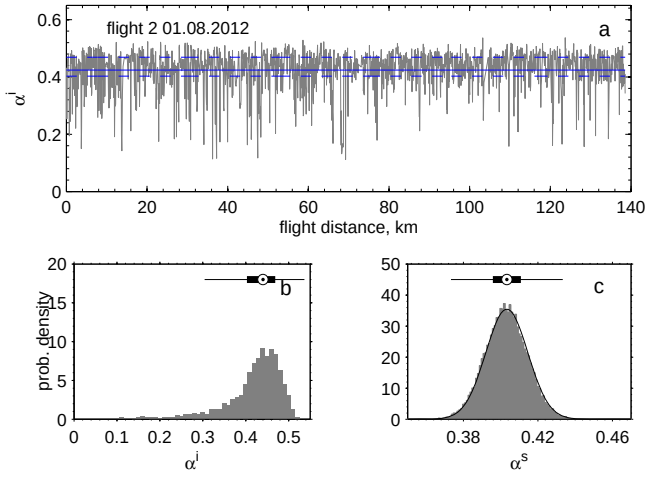

Figure 7. (a) Image-based aggregate surface albedo (α^i) along flight track 2 shown in Fig. 3. Solid blue line is for the image-based track average albedo of 0.42, and dashed lines show the quartiles $Q_{1,3}$ of (0.40,0.47) of the respective α^i probability density shown in **(b)**. Note skewness of the distribution towards lower albedo values and asymmetric position of the mean with respect to the 25 and 75 %; **(c)** bootstrap swath-based aggregate albedo α^s probability density, and the solid line shows the fitted normal pdf $\mathcal{N}(0.40, 0.01^2)$. The box plots on **(b)** and **(c)** use the same conventions as in Fig. 4.

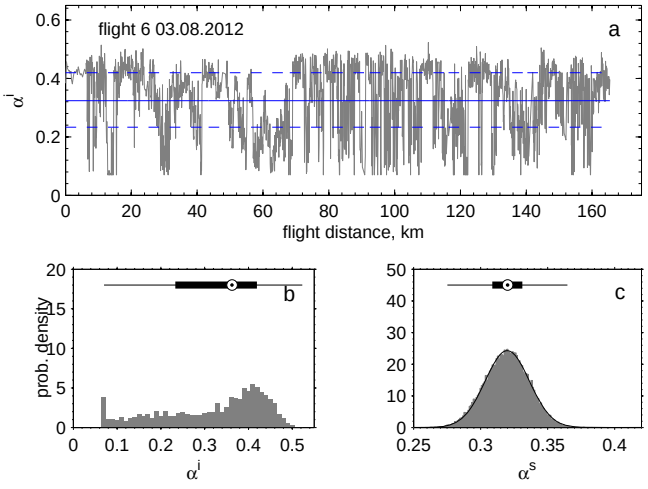

Figure 8. Same as in Fig. 7 but for flight 6 shown in Fig. 3. Solid blue line is for the image-based track average albedo of 0.32, and dashed lines show the 25 and 75 % (0.23,0.42) of the respective α^i probability density shown in **(b)**; **(c)** bootstrap swath-based aggregate albedo α^s probability density, and solid line shows the fitted normal pdf $\mathcal{N}(0.32, 0.02^2)$.

varied in the range of 0.78–0.88, whereas the probability of retaining the "open-water" state was lower: 0.51–0.57. These results are summarized in Table 3. The block length K was calculated as a ratio of N/N_{eff}, yielding a block size of 9–12 images for four of the six transects, which corresponded to approximately 500–700 m of the flight track. For the tracks with the lowest (flight 1) and highest (flight 6) open-water fractions the derived block lengths were 18 and 7 images, respectively.

For all tracks the α^s probability density is approximately Gaussian, with 95 % confidence according to the Lilliefors goodness-of-fit test of composite normality (Conover, 1999). The respective fits are shown together with the bootstrap pdfs in Figs. 7c, 8c, S2, S4, S6 and S8. The calculated standard deviations of the fitted Gaussian distributions are $\sigma_{\alpha^s} = 0.01$ for flights 1–5 and $\sigma_{\alpha^s_6} = 0.02$ for flight 6.

Flight tracks 1–5 demonstrate similar values of the swath-based aggregate albedo α^s of about 0.39, all lying within the estimated confidence intervals (see Table 2). This suggests that the data from these five flights can be combined to provide the regional-scale albedo estimate for the ice pack outside the MIZ. This is implemented using the same technique applied to the concatenated sequence of $\left\{f^i_{\text{mp}},\ f^i_{\text{ow}},\ S^i\right\}$ for all flight tracks but flight 6. When flight 6, representing mainly the marginal ice zone, is included in calculations, it decreases α^r to a value of 0.37. The latter is related to the presence of extensive open-water areas in the some

Table 3. Auxiliary data for the processed flight tracks used in the calculation of the flight-track albedo. $\mathbf{T}_{11}$ and $\mathbf{T}_{21}$ denote elements of the transition matrix of the fitted first-order Markov model and the respective estimated image block lengths.

Flight number	$\mathbf{T}_{11}$ $\phi_{\text{ice}\to\text{ice}}$	$\mathbf{T}_{21}$ $\phi_{\text{ow}\to\text{ow}}$	block length
1	0.88	0.57	18
2	0.83	0.53	12
3	0.78	0.48	8
4	0.80	0.49	9
5	0.82	0.52	10
Regional aggregate	0.82	0.51	10
6	0.76	0.25	7

30 km wide MIZ. The results of calculations are presented in Fig. 9a, and Table 2 further summarizes the results of the analysis.

The effect of open-water areas on the spatial albedo is demonstrated in Fig. 9b showing the bootstrap pdfs of sea-ice albedo α^s_{si} for tracks 1–6. We note that the spread in the inferred α^s_{si} pdfs between the individual tracks is much less pronounced compared to the respective α^s. The regional bootstrap α^r_{si} of about 0.44 thereby provides a good estimate of the albedo for melting sea ice about 0.7–0.9 m thick for the entire study area.

The data on f_{ow} and f_{mp}, merged from all six flights, were further binned in 0.1° wide latitudinal bins in a way similar to what was presented in Sect. 3.1. We calculated the bootstrap areal and sea-ice albedo for each latitudinal subset to yield the latitudinal distribution of these quantities. Figure 10

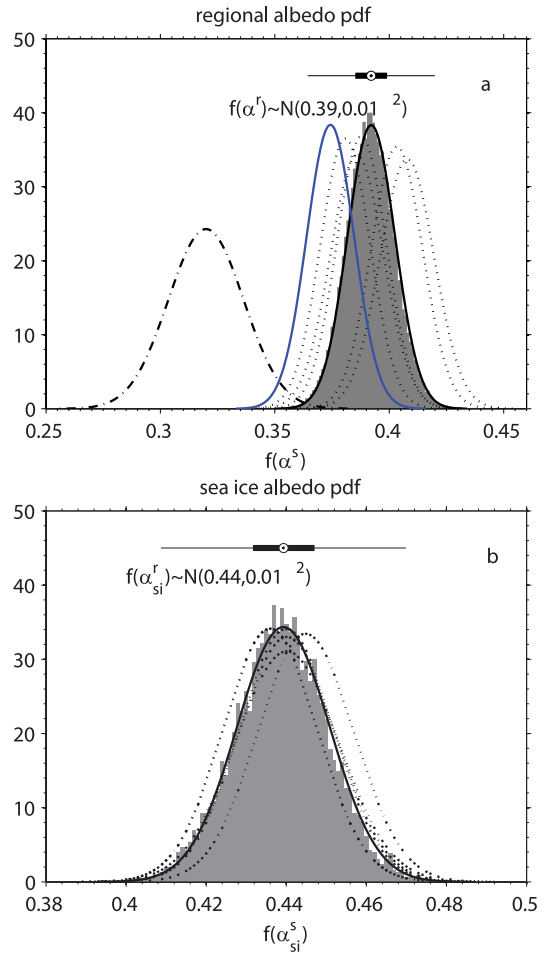

Figure 9. Regional **(a)** and sea-ice **(b)** bootstrap albedo pdfs obtained from merging the data from flights 1–5 **(a)** and 1–6 **(b)**. Solid black lines highlight the fitted Gaussian pdf with the parameters indicated in the panel. Dotted black lines show for the reference the fitted Gaussian pdfs for α^s from flights 1–5 **(a)** and 1–6 **(b)**. Black dash-dotted and solid blue lines in **(a)** also show the bootstrap albedo pdfs for flight 6 and the regional albedo derived from merging the data from all 6 flights together, respectively. The box plots on the top of the panels use the same conventions as in Fig. 4.

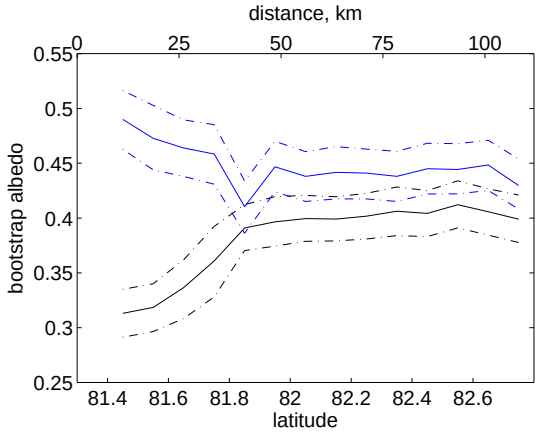

Figure 10. Latitudinal distribution in areal (black) and sea-ice (blue) bootstrap albedo derived from the six flight tracks. Dash-dotted lines show the respective 95 % confidence intervals on the estimate.

presents the results, demonstrating fairly stable values of α^s and α^s_{si} for the area outside the MIZ, in accordance with the corresponding results on f_{ow} and f_{mp} from Fig. 6. Within the MIZ increasing (decreasing) values of f_{ow} (f_{mp}) towards the ice edge drive opposite trends in the bootstrap albedos α^s and α^s_{si}. This suggests that a decrease in melt-pond fraction towards the ice edge may have a weak compensating effect on the areal albedo, slowing down the sea-ice surface melt in the MIZ. For solar radiation conditions observed during the drift experiment (Hudson et al., 2013), the net effect of increasing the sea-ice albedo to about 0.5 would be to remove roughly 5 W m^{-2} of solar energy input, enough to reduce melt by about 1.5 cm of pure ice over the period of the experiment. One should note, however, that the upscaling results in this area with a more intense bottom and lateral sea-ice melt should be interpreted with caution. Potential for bias in the EM sea-ice thickness measurements due to effects of open water in the footprint of the EM instrument and a large dependence of sea-ice albedo on thickness for the thinner ice makes the application of the in situ albedo measurements made outside the MIZ less certain.

In order to infer the relative contribution of the spatial variability in melt-pond/open-water coverage and the uncertainty of in situ albedo measurements to the overall variance of the swath-based and regional albedo estimates, we also repeated the numerical experiments with the albedo of surface types treated as constants. The result demonstrated a substantial reduction in the standard deviations σ_{α^s} and σ_{α^r} down to 0.003 and 0.002, respectively. This indicates that in the defined framework, about 90 % of the estimated variance of α^s and 95 % in α^r is due to variability and uncertainties in the in situ albedo measurements. Only a minor part of the variance is due to all other errors and variability accounted for in the model.

3.3 Assessing the aggregate scale for ICE camera imagery

The notion of aggregate scale for an environmental variable refers to the minimal spatial scale at which the contribution of local sampling variability to its total variance is diminished (Moritz et al., 1993). The concept is directly related to the weak law of large numbers, provided that the samples are drawn from a stationary distribution. Knowledge of this scale is crucial for an accurate upscaling of local measurements and subsequently linking them to larger-scale climate models. We note that in a hierarchy of spatial scales, the present study focuses specifically on the range of meters to hundreds

of kilometers, which encompasses the scales typical for in situ measurements up to regional models and CGCM.

The aggregate scale for the regional albedo was estimated using sets of (pseudo-)independent samples of different size drawn from the whole collection of classified images. The sample size varied from 10 to 1000 images, and for each sample size 10 000 subsets were drawn at random, without replacement, to gain the necessary statistics on the aggregate albedo distribution as a function of sample size and total sample area. As the image areas within each sample were not identical due to variations in the flight altitude, the average total area for each sample size was used. Images with an area over 6000 m^2, corresponding to a flight altitude above 55 m, were not included in the analysis.

Figure 11 (black lines) shows the fraction of sample-based aggregate albedo estimates, falling within the interval of ± 1 and ± 2 standard deviations of the regional aggregate albedo (Table 2), as a function of sample area. The results demonstrate a rapid growth in the proportion of accurate estimates of the regional albedo with an increase in the number of images drawn for analysis. The curves level out when the total sample area exceeds the threshold of about 0.7 km^2, when some 95 % of the subset-based estimates lie within the interval of 2 SD of the regional bootstrap albedo. One should emphasize that these estimates are specific to this study's setup, time period and region. For the range of flight altitudes typically sustained during the operation of the EM bird, the 0.7 km^2 aggregate scale corresponds to a set of at least 300 independent images spatially representative of the study region.

In order to simulate higher flight altitudes and examine the effect of smaller sample sets and/or sub-kilometer scale spatial autocorrelation in the state of sea-ice cover on the estimate of the aggregate scale, the numerical experiment was repeated with successive images combined into blocks of different length. The validity of this experiment relies on the assumption of smaller-scale anisotropy in statistical properties of the sea-ice surface. The red and grey lines in Fig. 11 show the fraction of the accurate estimates of the regional albedo for image blocks of length 10 and 25 images, respectively. Results suggest an increase in the aggregate scale to values above 2 km^2 which would correspond to sets of at least 80 (30) area-representative images captured from an altitude of about 100 (170) m. Notably the estimated thresholds (aggregate scales) have an order of magnitude similar to the respective estimate of > 1 km^2 obtained by Perovich et al. (2002b) during the SHEBA experiment in a different region of the Arctic.

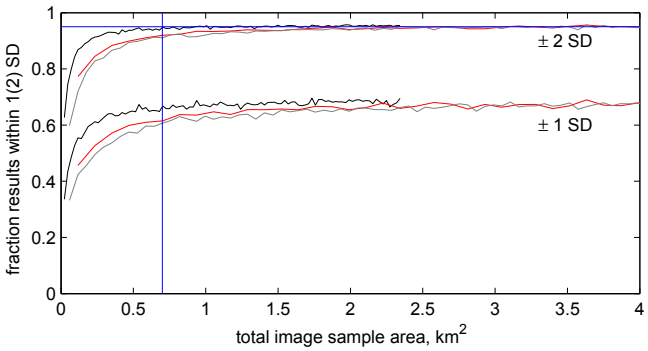

Figure 11. Fraction of image subset-based aggregate albedo values within the interval of ± 1 and ± 2 SD of the bootstrap estimated regional albedo as a function of total image (sample) area. The subsets are formed of image blocks of length 1 (black), 10 (red) and 25 (grey) images. The solid blue lines highlight the 0.95 fraction and 0.7 km^2 aggregate scale for subsets formed of single image blocks.

4 Conclusions

The formation of melt ponds on summer sea ice alters its optical properties over a broad range of wavelengths. This has implications for the surface energy balance and summer sea-ice decay as well as for practical issues of the remote sensing of sea ice. The study of sea-ice topography and the associated processes at these smaller scales was therefore identified to be of crucial importance for a better understanding of the seasonal evolution of the ice pack at a pan-Arctic scale and improvement of sea-ice parameterizations in GCMs (Eicken et al., 2004). Yet the considerable regional and intraseasonal variability of summer first-year ice albedo stipulates the need for further regional-scale studies of this parameter and its relation to other key physical factors characterizing the current state of sea-ice cover. Moreover, the recent progress made in the area of field data assimilation suggests even the regional-scale studies similar to the one presented here can potentially be valuable for improving the skills of GCMs in making seasonal sea-ice forecasts (Schröder et al., 2014; Castro-Morales et al., 2014).

Analysis of imagery and EM bird ice-thickness data from six low-altitude ice-survey flights conducted during the ICE12 drift experiment north of Svalbard at 82.3° N in late July/early August 2012 revealed a regional-scale homogeneity in the state of ice cover in the area of the drift track outside the MIZ. Within this area, with an extent of ≈ 150 km, the observed melt-pond fraction varied from 15 to 36 % in 50 % of cases, around the median of $f^i_{\rm mp}$=26 %, relative to the sea-ice area. Accounting for the inferred bias of the image-processing technique, a value of $f^i_{\rm mp} = 29$ % should be considered a realistic regional estimate for the 70–90 cm thick ice observed during the campaign. We note that in some occasions the melt ponds could cover as much as 66 % of the ice surface. For some 10 % of images with sea ice in the field of view, the sea-ice surface exhibited no or very little melt-pond coverage ($f^i_{\rm mp} < 4$ %), possibly associated with the snow-free sea ice formed in the leads late in the winter season (Eicken et al., 2004). Within the 30 km wide MIZ, $f^i_{\rm mp}$ showed a decline towards the ice edge to an average value

below 10 %, which we linked to more intense melt leading to a transformation of melt ponds into open water and to a decrease in the typical floe size.

The regional spatial albedo and albedo of pack ice have been obtained from the observational data on the distribution of surface types and the respective broadband albedos using the block bootstrap technique. The method implicitly accounts for uncertainties due to sampling in the spatial domain with a priori unknown variability, surface type classification errors and in situ albedo measurements. The set of more than 10 000 classified images representing a total of 28 km^2, combined with a series of in situ broadband albedo measurements conducted on sea ice, was used to produce the regional aggregate albedo estimate of 0.37 (0.35; 0.40). Elimination of the MIZ with its higher open-water fraction from the computations would increase α^{r} to a value of 0.39 (0.37; 0.41), still within the estimated confidence bounds. The respective value of $\alpha^{\mathrm{r}}_{\mathrm{si}}$ of 0.44 (0.42; 0.46) for the observed first-year pack ice shows little dependence on the data subset used. The inferred homogeneous latitudinal distribution of both α^{r} and $\alpha^{\mathrm{r}}_{\mathrm{si}}$ reflects the homogeneity of the melt-pond and open-water fractions in the study area. The tendency towards decreasing α^{r} and increasing $\alpha^{\mathrm{r}}_{\mathrm{si}}$ is observed only within the MIZ, as a result of corresponding changes in f_{mp} and f_{ow}.

The regional melt-pond fraction observed in this campaign is well within the range of variability of this parameter that was reported in the previous studies on the topic both for the multiyear and first-year ice, including landfast ice, in a similar stage of melt (e.g., Fetterer and Untersteiner, 1998; Tschudi et al., 2001; Perovich et al., 2002b, 2009; Eicken et al., 2004, see also a summary on previous observations in Polashenski et al., 2012). We also observe a consistency with the decadal (2000–2011) average of the remote sensing based retrievals of this parameter for the corresponding latitude and period of the year (Rösel et al., 2012); yet the termination of the data set in 2011 prevented us from making a direct comparison for the study area.

Analysis of the relevant literature indicates that our aggregate albedo estimates are systematically lower than the values for melting FYI reported in a number of other ship-based and aerial studies from matching latitudes and this time of year. The bare level ice albedo of 0.55 we used is lower than the estimates of 0.6–0.65 typically used for bare first-year ice (e.g., Grenfell and Maykut, 1977; Grenfell and Perovich, 2004), which is most likely to be attributed to the thinner, 70–90 cm thick, ice we observed. The melt-pond albedo (specifically prevalent dark ponds) measured during the campaign was already at the lower edge of previously observed values of 0.1–0.4 (e.g., Tschudi et al., 2001; Perovich et al., 2002b, a; Lu et al., 2010) as well as analytical approximations (Makshtas and Podgorny, 1996). Since the pond formation during melt is considered the main mechanism driving an overall decrease of the aggregate sea-ice albedo, we attribute a generally lower value of $\alpha^{\mathrm{r}}_{\mathrm{si}} = 0.44$ to a late melt stage and the associated darker ponds on the surface. The lower aggregate albedo of melting first-year ice of 0.37 reported by Nicolaus et al. (2012) based on the results of the trans-Arctic cruise ARK-XXVI/3 in 2011 and measured albedos from Perovich (1996) is related to a substantially higher first-year ice melt-pond fraction (0.43) that we did not observe in our study. This discrepancy nevertheless highlights a substantial regional and intraseasonal/interannual variability in the parameters used in upscaling to a regional aggregate estimate. We note also that the derived relatively low values for a regional melting first-year ice albedo highlights the need for a reassessment/improvement of many existing albedo parameterizations used in the sea-ice modules of GCMs. Although it has been identified as one of the research priorities more than a decade ago (e.g., Curry et al., 2001; Eicken et al., 2004), a number of models still rely on far too high albedos for melting first-year ice (see e.g., Johnson et al., 2012), with implications for the modeled seasonal sea-ice cycle.

The use of a large collection of classified images from the area allowed an assessment of the aggregate scale for the regional albedo of about 0.7 km^2, which corresponds to at least 300 representative images of the study area captured by the ICE camera setup from an altitude of 35–40 m. Higher flight altitudes would require fewer classified images, though the area covered must be larger. We emphasize that these estimates are linked with the setup configuration used as well as the state of sea-ice cover during the ICE12 experiment. This result suggests that gaining adequate regional statistics on $f^{\mathrm{s}}_{\mathrm{ow}}$, $f^{\mathrm{s}}_{\mathrm{mp}}$ and hence α^{r}, provided a spatial homogeneity of sea ice, would require a relatively limited number of processed images, with implication for the labor intensity of the procedure.

The results indicate that about 95 % of the uncertainty in our regional albedo estimate is due to variability in the in situ albedo measurements. This variability is related to both the natural local variability of this parameter due to, e.g., underlying ice thickness or pond depth, as well as to the uncertainty stemming from the measurement technique itself. This indicates the need for a series of local measurements carried out for each surface category as a necessary prerequisite for a high-quality regional upscaling. A particular focus should be on melt-pond albedo evolution at the latter stages of ice decay, when the ice beneath the ponds gets thin, the ponds begin to melt through, and their albedo approaches that of open water.

Processing and analysis of the data from 2012 is an ongoing effort. The plans for further work include a detailed analysis of the spatial melt-pond distribution and a joint analysis of EM bird ice thickness data, optical melt pond characteristics and ridging of sea ice. As the setup was designed to enable the capability of producing 3-D reconstructions of the sea-ice surface topography, some scenes were selected for a detailed analysis of the surface morphology. Gaining statistics on small-scale sea-ice topography is considered necessary (Eicken et al., 2004) for better understanding and modeling the evolution of first-year ice during melt.

The Supplement related to this article is available online at doi:10.5194/tc-9-255-2015-supplement.

Acknowledgements. We thank the crew of R/V *Lance* and Airlift as well as other scientists and engineers on board for their assistance in carrying out the measurements. Funding was provided by the Centre for Ice, Climate and Ecosystems (ICE) at the Norwegian Polar Institute via the ICE-Fluxes project. This work was also supported by ACCESS, a European project within the Ocean of Tomorrow call of the European Commission Seventh Framework Programme, grant no. 265863, and the Research Council of Norway through the EarthClim (207711/E10) project. M. Nicolaus (AWI, Bremerhaven) and an anonymous reviewer are acknowledged for their constructive comments on the first version of the manuscript.

Edited by: M. van den Broeke

References

Björk, G., Stranne, C., and Borenäs, K.: The Sensitivity of the Arctic Ocean Sea Ice Thickness and Its Dependence on the Surface Albedo Parameterization, J. Climate, 26, 1355–1370, doi:10.1175/JCLI-D-12-00085.1, 2013.

Castro-Morales, K., Kauker, F., Losch, M., Hendricks, S., Riemann-Campe, K., and Gerdes, R.: Sensitivity of simulated Arctic sea ice to realistic ice thickness distributions and snow parameterizations, J. Geophys. Res.-Oceans, 119, 559–571, doi:10.1002/2013JC009342, 2014.

Conover, W.: Practical nonparametric statistics, Wiley series in probability and statistics, Wiley, New York, USA, 3rd edn., 584 pp., 1999.

Curry, J. A., Schramm, J. L., and Ebert, E. E.: Sea Ice-Albedo Climate Feedback Mechanism., J. Climate, 8, 240–247, doi:10.1175/1520-0442(1995)008<0240:SIACFM>2.0.CO;2, 1995.

Curry, J. A., Schramm, J. L., Perovich, D. K., and Pinto, J. O.: Applications of SHEBA/FIRE data to evaluation of snow/ice albedo parameterizations, J. Geophys. Res.-Atmos., 106, 15345–15355, doi:10.1029/2000JD900311, 2001.

Derksen, C., Piwowar, J., and LeDrew, E.: Sea-Ice Melt-Pond Fraction as Determined from Low Level Aerial Photographs, Arctic Alpine Res., 29, 345–351, 1997.

Doronin, Y. and Kheisin, D.: Sea Ice, Amerind Publishing Company, Office of Polar Programs and the National Science Foundation, Washington D.C., USA, 323 pp., 1977.

Efron, B. and Tibshirani, R.: An introduction to the bootstrap, CRC press, New York, USA, 57, 456 pp., 1993.

Eicken, H., Krouse, H. R., Kadko, D., and Perovich, D. K.: Tracer studies of pathways and rates of meltwater transport through Arctic summer sea ice, J. Geophys. Res.-Oceans, 107, 8046, doi:10.1029/2000JC000583, 2002.

Eicken, H., Grenfell, T. C., Perovich, D. K., Richter-Menge, J. A., and Frey, K.: Hydraulic controls of summer Arctic pack ice albedo, J. Geophys. Res.-Oceans, 109, C08007, doi:10.1029/2003JC001989, 2004.

Fetterer, F. and Untersteiner, N.: Observations of melt ponds on Arctic sea ice, J. Geophys. Res.-Oceans, 103, 24821–24835, doi:10.1029/98JC02034, 1998.

Gonzalez, R. C., Woods, R. E., and Eddins, S. L.: Digital Image Processing using MATLAB, Gatesmark Publishing, USA, 2nd edition, 827 pp., 2009.

Grenfell, T. C. and Maykut, G. A.: The optical properties of ice and snow in the Arctic Basin, J. Glaciol., 18, 445–463, 1977.

Grenfell, T. C. and Perovich, D. K.: Seasonal and spatial evolution of albedo in a snow-ice-land-ocean environment, J. Geophys. Res.-Oceans, 109, C01001, doi:10.1029/2003JC001866, 2004.

Haas, C., Lobach, J., Hendricks, S., Rabenstein, L., and Pfaffling, A.: Helicopter-borne measurements of sea ice thickness, using a small and lightweight, digital EM system, J. Appl. Geophys., 67, 234–241, doi:10.1016/j.jappgeo.2008.05.005, 2009.

Hanesiak, J. M., Barber, D. G., de Abreu, R. A., and Yackel, J. J.: Local and regional albedo observations of arctic first-year sea ice during melt ponding, J. Geophys. Res.-Oceans, 106, 1005–1016, doi:10.1029/1999JC000068, 2001.

Hohenegger, C., Alali, B., Steffen, K. R., Perovich, D. K., and Golden, K. M.: Transition in the fractal geometry of Arctic melt ponds, The Cryosphere, 6, 1157–1162, doi:10.5194/tc-6-1157-2012, 2012.

Holland, M. M., Bailey, D. A., Briegleb, B. P., Light, B., and Hunke, E.: Improved Sea Ice Shortwave Radiation Physics in CCSM4: The Impact of Melt Ponds and Aerosols on Arctic Sea Ice, J. Climate, 25, 1413–1430, doi:10.1175/JCLI-D-11-00078.1, 2012.

Hudson, S. R., Granskog, M. A., Karlsen, T. I., and Fossan, K.: An integrated platform for observing the radiation budget of sea ice at different spatial scales, Cold Reg. Sci. Technol., 82, 14–20, doi:10.1016/j.coldregions.2012.05.002, 2012.

Hudson, S. R., Granskog, M. A., Sundfjord, A., Randelhoff, A., Renner, A. H. H., and Divine, D. V.: Energy budget of first-year Arctic sea ice in advanced stages of melt, Geophys. Res. Lett., 40, 2679–2683, doi:10.1002/grl.50517, 2013.

Johnson, M., Proshutinsky, A., Aksenov, Y., Nguyen, A. T., Lindsay, R., Haas, C., Zhang, J., Diansky, N., Kwok, R., Maslowski, W., Häkkinen, S., Ashik, I., and de Cuevas, B.: Evaluation of Arctic sea ice thickness simulated by Arctic Ocean Model Intercomparison Project models, J. Geophys. Res.-Oceans, 117, C00D13, doi:10.1029/2011JC007257, 2012.

Karlsson, J. and Svensson, G.: Consequences of poor representation of Arctic sea-ice albedo and cloud-radiation interactions in the CMIP5 model ensemble, Geophys. Res. Lett., 40, 4374–4379, doi:10.1002/grl.50768, 2013.

Kim, D.-J., Hwang, P., Chung, K., Lee, S., Jung, H.-S., and Moon, W.: Melt pond mapping with high-resolution SAR: the first view, Proc. IEEE, 101, 748–758, doi:10.1109/JPROC.2012.2226411, 2013.

Kunsch, H. R.: The Jackknife and the Bootstrap for General Stationary Observations, Ann. Stat., 17, 1217–1241, doi:10.1214/aos/1176347265, 1989.

Lu, P., Li, Z., Cheng, B., Lei, R., and Zhang, R.: Sea ice surface features in Arctic summer 2008: Aerial observations, Remote Sens. Environ., 114, 693–699, doi:10.1016/j.rse.2009.11.009, 2010.

Makshtas, A. and Podgorny, I.: Calculation of melt pond albedos on arctic sea ice, Polar Res., 15, 43–52, 1996.

Markus, T., Cavalieri, D. J., Tschudi, M. A., and Ivanoff, A.: Comparison of aerial video and Landsat 7 data over ponded sea

ice, Remote Sens. Environ., 86, 458–469, doi:10.1016/S0034-4257(03)00124-X, 2003.

MATLAB: version 8.0.0.783 (R2012b), The MathWorks Inc., Natick, Massachusetts, USA, 2012.

Maykut, G.: Large-Scale Heat Exchange and Ice Production in the Central Arctic, J. Geophys. Res., 87, 7971–7984, 1982.

Mitchell, J., Dzerdzeevskii, B., and Flohn, H.: Climatic change: report of a working group of the Commission for Climatology, Technical Note 79, World Meteorological Organisation, 1966.

Moritz, R. E., Curry, J., Thorndike, A., and Untersteiner, N.: SHEBA: a Research Program on the Surface Heat Budget of the Arctic Ocean, Report 3, Arctic Syst. Sci.: Ocean-Atmos.-Ice Interact., 34 pp., 1993.

Nazintsev, Y.: The heat balance of the surface of the multiyear ice cover in the central Arctic, Trudy AANII, 267, 110–126, 1964 (in Russian).

Nicolaus, M., Katlein, C., Maslanik, J., and Hendricks, S.: Changes in Arctic sea ice result in increasing light transmittance and absorption, Geophys. Res. Lett., 39, L24501, doi:10.1029/2012GL053738, 2012.

Nychka, D., Buchberger, R., Wigley, T., Santer, B. D., Taylor, K. E., and Jones, R. H.: Confidence Intervals for Trend Estimates With Autocorrelated Observations (unpublished manuscript), available at: http://citeseerx.ist.psu.edu/viewdoc/download?doi=10.1.1.33.6828&rep=rep1&type=pdf (last access: 4 February 2015), 2000.

Otsu, N.: A Threshold Selection Method from Gray-Level Histograms, Systems, Man and Cybernetics, IEEE T. Syst. Man. Cyb., 9, 62–66, doi:10.1109/TSMC.1979.4310076, 1979.

Pegau, S. W. and Paulson, C. A.: The albedo of Arctic leads in summer, Ann. Glaciol., 33, 221–224, doi:10.3189/172756401781818833, 2001.

Perovich, D. K.: The optical properties of sea ice, US Army Corps of Engineers, Cold Regions Research & Engineering Laboratory, 33 pp., available at: www.dtic.mil/cgi-bin/GetTRDoc?AD=ADA310586, 1996.

Perovich, D. K.: On the aggregate-scale partitioning of solar radiation in Arctic sea ice during the Surface Heat Budget of the Arctic Ocean (SHEBA) field experiment, J. Geophys. Res.-Oceans, 110, C03002, doi:10.1029/2004JC002512, 2005.

Perovich, D. K. and Polashenski, C.: Albedo evolution of seasonal Arctic sea ice, Geophys. Res. Lett., 39, L08501, doi:10.1029/2012GL051432, 2012.

Perovich, D. K., Grenfell, T. C., Light, B., and Hobbs, P. V.: Seasonal evolution of the albedo of multiyear Arctic sea ice, J. Geophys. Res.-Oceans, 107, SHE 20-1–SHE 20-13, doi:10.1029/2000JC000438, 2002a.

Perovich, D. K., Tucker, W. B., and Ligett, K. A.: Aerial observations of the evolution of ice surface conditions during summer, J. Geophys. Res.-Oceans, 107, SHE 24-1–SHE 24-14, doi:10.1029/2000JC000449, 2002b.

Perovich, D. K., Grenfell, T. C., Light, B., Elder, B. C., Harbeck, J., Polashenski, C., Tucker, W. B., and Stelmach, C.: Transpolar observations of the morphological properties of Arctic sea ice, J. Geophys. Res.-Oceans, 114, C00A04, doi:10.1029/2008JC004892, 2009.

Petrich, C., Eicken, H., Polashenski, C. M., Sturm, M., Harbeck, J. P., Perovich, D. K., and Finnegan, D. C.: Snow dunes: A controlling factor of melt pond distribution on Arctic sea ice, J. Geophys. Res.-Oceans, 117, C09029, doi:10.1029/2012JC008192, 2012.

Polashenski, C., Perovich, D., and Courville, Z.: The mechanisms of sea ice melt pond formation and evolution, J. Geophys. Res.-Oceans, 117, C01001, doi:10.1029/2011JC007231, 2012.

Renner, A. H., Dumont, M., Beckers, J., Gerland, S., and Haas, C.: Improved characterisation of sea ice using simultaneous aerial photography and sea ice thickness measurements, Cold Reg. Sci. Technol., 92, 37–47, doi:10.1016/j.coldregions.2013.03.009, 2013.

Rösel, A., Kaleschke, L., and Birnbaum, G.: Melt ponds on Arctic sea ice determined from MODIS satellite data using an artificial neural network, The Cryosphere, 6, 431–446, doi:10.5194/tc-6-431-2012, 2012.

Schröder, D., Feltham, D. L., Flocco, D., and Tsamados, M.: September Arctic sea-ice minimum predicted by spring melt-pond fraction, Nat. Climate Change, 4, 353–357, doi:10.1038/nclimate2203, 2014.

Tschudi, M. A., Curry, J. A., and Maslanik, J. A.: Airborne observations of summertime surface features and their effect on surface albedo during FIRE/SHEBA, J. Geophys. Res, 106, 15335–15344, doi:10.1029/2000JD900275, 2001.

Tschudi, M. A., Maslanik, J. A., and Perovich, D. K.: Derivation of melt pond coverage on Arctic sea ice using MODIS observations, Remote Sens. Environ., 112, 2605–2614, doi:10.1016/j.rse.2007.12.009, 2008.

Untersteiner, N.: On the mass and heat budget of arctic sea ice, Archiv für Meteorologie, Geophysik und Bioklimatologie, Serie A, 12, 151–182, doi:10.1007/BF02247491, 1961.

World Meteorological Organization: WMO sea-ice nomenclature. Terminology, codes and illustrated glossary, Secretariat of the World Meteorological Organization Geneva, Switzerland, 147 pp., 1970.

Zubov, N.: Arctic Ice, Izd. Glavsevmorputi, Moscow, (translated by US Navy Oceanographic Office, Springfield, 1963), 360 pp., 1945.